Optical tracking of deep-space spacecraft in Halo L2 orbits and beyond: the Gaia mission as a pilot case☆

Alberto Buzzoni*, Giuseppe Altavilla, Silvia Galleti

INAF - Osservatorio Astronomico di Bologna, Via Ranzani 1 40127 Bologna Italy

Abstract

We tackle the problem of accurate optical tracking of distant man-made probes, on Halo orbit around the Earth-Sun libration point L2 and beyond, along interplanetary transfers. The improved performance of on-target tracking, especially when observing with small-class telescopes is assessed providing a general estimate of the expected S/N ratio in spacecraft detection. The on-going Gaia mission is taken as a pilot case for our analysis, reporting on fresh literature and original optical photometry and astrometric results.

The probe has been located, along its projected nominal path, with quite high precision, within $0.13_{\pm 0.09}$ arcsec, or $0.9_{\pm 0.6}$ km. Spacecraft color appears to be red, with $(V - R_c) = 1.1_{\pm 0.2}$ and a bolometric correction to the R_c band of $(Bol - R_c) = -1.1_{\pm 0.2}$. The apparent magnitude, $R_c = 20.8_{\pm 0.2}$, is much fainter than originally expected. These features lead to suggest a lower limit for the Bond albedo $\alpha = 0.11_{\pm 0.05}$ and confirm that incident Sun light is strongly reddened by Gaia through its on-board MLI blankets covering the solar shield.

Relying on the Gaia figures, we found that VLT-class telescopes could yet be able to probe distant spacecraft heading Mars, up to 30 million km away, while a broader optical coverage of the forthcoming missions to Venus and Mars could be envisaged, providing to deal with space vehicles of minimum effective area $\mathcal{A} \geq 10^6$ cm^2. In addition to L2 surveys, 2m-class telescopes could also effectively flank standard radar-ranging techniques in deep-space probe tracking along Earth's gravity-assist maneuvers for interplanetary missions.

Keywords: Space vehicles; Techniques: high angular resolution; Astrometry and celestial mechanics; Techniques: photometric

1. Introduction

The exploitation of the Sun-Earth Lagrangian points, especially L1 and L2, along the Sun-Earth direction (Farquhar & Kamel, 1973; Nariai, 1975; Rawal, 1991; Farquhar et al., 2002) has been an extraordinary challenge for space exploration in the recent years. For their particular position, some 1.5 10^6 km away, on opposite sides of Earth and therefore well beyond the Moon, both locations are ideal lookouts for astrophysical observatories aimed at studying the Sun (L1) and the deep Universe (L2), far from any anthropic contamination. The L2 point, in particular, has been hosting a number of important astrophysical missions, starting with the Wmap, Planck and Herschel probes, and currently continuing with the Gaia mission, aimed at performing an exhaustive census of the Milky Way stellar population (de Bruijne, 2012; Cacciari, 2015). Following Gaia, other major space facilities are planned to be located in a so-called Halo L2 orbit in the forthcoming years. These include the James-Webb Space Telescope (Jwst; Gardner et al., 2006), the Euclid cosmological probe (Laureijs et al., 2010), and the Athena X-ray observatory (Barret et al., 2013).

Optical ground tracking is yet of recognized importance for any L2 mission. For the co-rotating orbit to be maintained within its nominal figures, in fact, we need to carefully check spacecraft during its course along a complex Lissajous trajectory, as seen from Earth (e.g. Bray & Gouclas, 1967; Zagouras & Markellos, 1985; Liu et al., 2007; Kolemen et al., 2012; Dutt & Sharma, 2011; Qiao et al., 2014). This is also of special interest for any space observatory (like Gaia, or the next Jwst) as its absolute inertial position is required with exquisite precision to allow, for instance, a confident measure of astronomical parallaxes of distant stars with the on-board instruments. In this regard, radar-ranging techniques may actually provide a better measurement of spacecraft distance and radial velocity (Imbriale, 2003), but telescope observations, from their side, take advantage of a superior angular resolution, providing in principle more accurate astrometry and finer proper motion estimates (Altmann et al., 2011).

Compared to the observation of near-Earth satellites,

☆Based on observations collected at the Cassini Telescope of the Loiano Observatory, Italy

*Corresponding author:

Email address: alberto.buzzoni@oabo.inaf.it (Alberto Buzzoni)

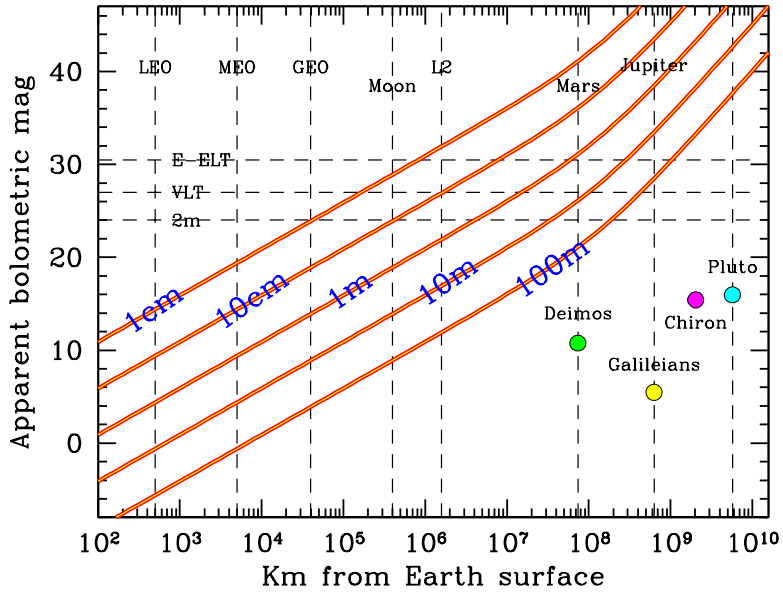

Figure 1: The apparent bolometric magnitude for man-made spacecraft at increasing distance from Earth, according to eq. (2). Probe scale-size is labelled along each curve. The altitude of LEO (set to 500 km), MEO (5000 km) and GEO terrestrial orbits is marked, together with a few small bodies in the Solar System and their reference interplanetary distances at Earth's opposition. The limiting magnitude reached by a 2m mid-class telescope, the 8m ESO VLT and the forthcoming 40m E-ELT telescope, when observing distant Sun-type stars, is also sketched on the plot.

however, optical tracking of distant probes, in L2 and on route to even farther interplanetary distances, has to deal with much fainter target magnitudes, a drawback that urges a substantial improvement in terms of telescope skills and especially of observing techniques to effectively assess our deep-space situational awareness (e.g. Mooney et al., 2006; Ruprecht et al., 2014; Woods et al., 2014).

In this contribution we want therefore to briefly assess some technical issues (Sec. 2) dealing with accurate ground tracking of deep-space probes at optical wavelength, taking fresh observations of the Gaia spacecraft (Sec. 3) as a pilot case for tuning up our theoretical analysis. The relevant photometric figures for Gaia will constrain the required telescope performance, for the optical observations to consistently complement standard radar-tracking techniques as in the forthcoming space missions to Mars and other planets of the solar system (Sec. 4). Our conclusions will be briefly stressed in Sec. 5.

2. Apparent magnitude of distant spacecraft

Depending on its physical properties, a satellite under solar illumination reflects a fraction α (the so-called Bond albedo) of the incident flux. The remaining fraction of the input energy is retained and heats the body up to an equilibrium temperature that leads to a balance between the absorbed and re-emitted flux. At Earth's heliocentric distance, this temperature cannot exceed 120°C (e.g. Gilmore, 2002), so that thermal emission of spacecraft in the terrestrial neighborhood (and beyond) is only relevant at mid/far-infrared wavelength.

If a probe offers a cross-section s^2 to Sun's light, being s its reference scale-size, and if we assume the illuminated body to reflect isotropically, then the apparent bolometric magnitude of a spacecraft placed at a distance d from Earth's surface (at Sun's opposition)[1] simply scales as the ratio of the incident solar flux at Earth and at the spacecraft distance, so that

$$m_{\rm bol} - m_{\odot}^{\rm bol} = -2.5 \log \left[\left(\frac{D_{\odot}}{D_{\odot} + d} \right)^2 \left(\frac{s^2}{4\pi d^2} \right) \right], \quad (1)$$

where $D_{\odot} = 1.49\,10^{13}$ cm is the astronomical unit (AU) and $m_{\odot}^{\rm bol} = -26.85$ is the apparent bolometric magnitude of the Sun, as seen from Earth (e.g. Karttunen et al., 1996). With the relevant substitutions, and expressing the spacecraft distance $u = d/D_{\odot}$ in AU, eq. (1) takes the form:

$$m_{\rm bol} = -5 \log s + 5 \log[u\,(1+u)] + k, \quad (2)$$

where the numerical constant is

$$k = 2.5 \log(4\pi D_{\odot}^2) + m_{\odot}^{\rm bol} = 41.77, \quad (3)$$

providing the satellite scale-size s is set in cm.

In Fig. 1 we report an illustrative summary of the expected bolometric magnitude for distant man-made probes of different characteristic size, compared with a few small planetary bodies. Just as a guideline, the limiting magnitude as for observing Sun-type stars, reached by mid-class

[1] Although, strictly speaking, d is a topocentric distance, to all extent, for a distant spacecraft in L2 and beyond, it basically coincides with the geocentric distance, as well.

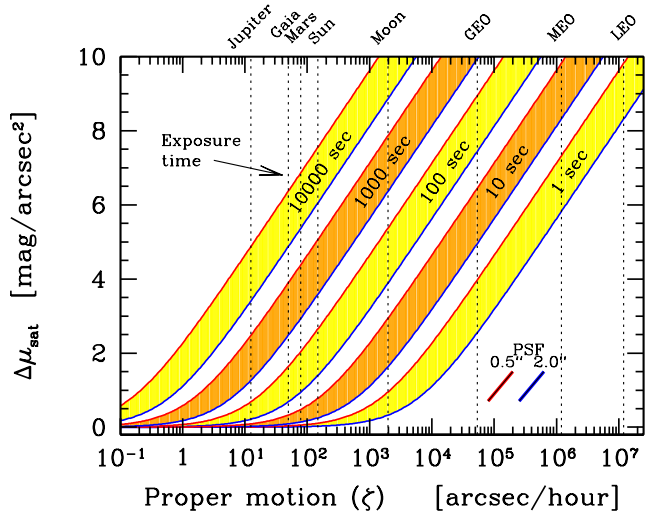

Figure 2: The surface-brightness dimming for trailing satellites, according to eq. (5). Different exposure times are assumed, as labelled. Each strip has a lower and upper envelope for a 2" and 0.5" FWHM seeing figure, respectively. The reference angular speed for satellites in LEO, MEO, and GEO (Veis, 1963) is reported together with the mean sky motion for other relevant solar bodies. In addition, we also display the mean angular velocity of spacecraft Gaia, along its Halo L2 orbit.

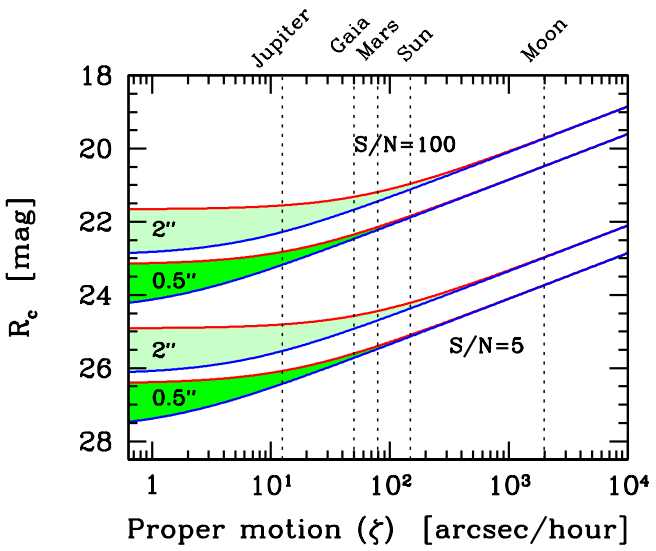

Figure 3: The magnitude limit reached by a 8m telescope, with a DQE = 0.8, at a 5 and 100 S/N detection level in 100 (upper envelope) and 1000 sec (lower envelope of the curves) exposure time, as from eq. (6). We assume to observe in the R_c band under two extreme seeing conditions, namely with a FWHM of 0.5 and 2.0 arcsec, and with a dark sky ($\mu^R_{\rm sky} = 20.5$ mag arcsec^{-2}). The indicative proper motion of some reference objects is reported, as from Fig. 2.

(2m aperture) and new-generation telescopes (i.e. the ESO 8m VLT and the forthcoming 40m E-ELT) is also marked on the plot.

As a fraction $(1-\alpha)$ of the incident solar flux is "diverted" into the infrared, to convert the bolometric figures to other broad-band *optical* magnitudes, say for instance the Johnson-Cousins R_c band, we have to dim the re-processed optical flux such as

$$m_R = m_{\rm bol} - BC'_R - 2.5\,\log\alpha, \qquad (4)$$

being $BC'_R = (m_{\rm bol} - m_R)$ the bolometric correction to the band, if satellite were a perfect acromatic reflector (i.e. for $\alpha \to 1$). This value has to be estimated on the basis of satellite's physical and geometrical properties. If we lack this information, then either the solar value ($BC'_R = +0.3$) could be taken as a first approximation or, if a color is known for our target, the BC'_R correction for a more appropriate star could be chosen, as from standard calibrations in the literature (e.g. Johnson, 1966; Bessell, 1979; Buzzoni et al., 2010).

2.1. Motion dimming

For fixed exposure time, any moving satellite tends to appear more elusive than fixed stars of the same magnitude on CCD images. In fact, while a star is supposed to concentrate most of its photons across a spot of area $a = \pi(\textsc{Fwhm}/2)^2$, whose FWHM depends on the telescope point-spread-function, a target moving with angular speed ζ, along a time $t_{\rm exp}$, would spread its light across a larger area $a' = \zeta\, t_{\rm exp}\,\textsc{Fwhm} + \pi(\textsc{Fwhm}/2)^2$. If both the star and the moving target have the same magnitude, the latter would actually be harder to catch, because of a lower mean surface brightness and a correspondingly poorer S/N ratio. The surface-brightness dimming can be quantified in

$$\Delta\mu_{\rm sat} = 2.5\log(a'/a) = 2.5\log\left(1 + \frac{4\,t_{\rm exp}\,\zeta}{\pi\textsc{Fwhm}}\right). \qquad (5)$$

Note that the effect does not depend on target magnitude. Rather, and quite interestingly, it becomes more severe with increasing exposure time and with improving seeing (that is for a better FWHM value), as shown in Fig. 2.

According to telescope diameter $\mathcal{D}$ and the exposure time $t_{\rm exp}$, the S/N ratio of a trailing object can eventually be computed as

$$\left(\frac{S}{N}\right)_{\rm trail} = \mathcal{R}\,10^{-0.4\left[m_{\rm sat} - \left(\frac{\mu_{\rm sky} - \Delta\mu_{\rm sat}}{2}\right)\right]}, \qquad (6)$$

with

$$\mathcal{R} = \frac{\mathcal{D}}{\textsc{Fwhm}}\,(n_o\,\textsc{Dqe}\,t_{\rm exp})^{1/2}. \qquad (7)$$

In previous equations, $\mu_{\rm sky}$ is sky surface brightness, n_o and DQE are the reference photon number for the magnitude zero point and the detector quantum efficiency, respectively, according to the photometric band of our observations. By definition, $n_o = (f_o\,\lambda_o\,\Delta_\lambda)/(h\,c)$, being f_o the zero-mag reference flux, λ_o and Δ_λ the effective wavelength and width of the photometric band, respectively, h the Planck constant and c the speed of light, as usual. For the R_c band, $n_o = 1.05\ 10^6$ photons cm^{-2} s^{-1} (Buzzoni, 2005). Notice that, if $\zeta \to 0$, then the $\Delta\mu_{\rm sat}$ term vanishes and eq. (6) approaches the S/N ratio for a fixed star.

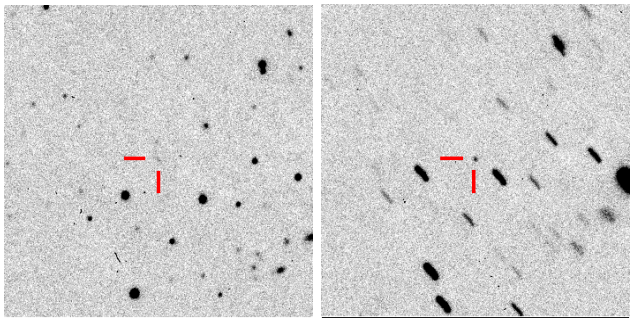

Figure 4: The spacecraft GAIA, as detected in the night of Oct 17-18, 2014 with the 1.52m telescope of the Loiano Observatory. The two panels are consecutive 300 sec exposures in "white" light (i.e. CCD with no photometric filter) of the same field with sideral (left) and differential (right) telescope tracking on. The displayed field is 3×3 arcmin across. North is up, East to the left. Pixel size is 0.58 arcsec. See text for a discussion.

As an illustrative case, in Fig. 3 we report the limiting magnitude in the R_c band, that can be achieved for a trailing target at a S/N = 5 and 100 detection level with a 8m telescope (DQE = 0.8) in a 100 and 1000 sec exposure time. We assume to observe from a good astronomical site ($\mu^R_{\rm sky} = 20.5$ mag arcsec^{-2}, e.g. Patat, 2003), under two extreme seeing conditions (namely 0.5" and 2.0" FWHM). An important feature of the plot is that mag limit for high-speed satellites does not depend on exposure time but it only improves with a better seeing or a bigger telescope. In the latter case, eq. (6) (and the curves in Fig. 3) offsets by $\Delta R_{\rm lim} = 2.5 \log(\mathcal{D}/800)$, by expressing $\mathcal{D}$ in cm.

3. The Gaia observations as a benchmark

Previous arguments make clear that, when observing distant spacecraft, *on-target* telescope tracking, such as to compensate target motion, is the mandatory requirement for letting any faint target literally "emerge" from the background noise. Compared to the output of eq. (6), in fact, the expected improvement in the S/N ratio for the latter case is of the order of

$$\left(\frac{S}{N}\right)_{\rm track} = \left(\frac{S}{N}\right)_{\rm trail} 10^{+0.2\,\Delta\mu_{\rm sat}}. \qquad (8)$$

As a striking example in this sense, we report here on two recent observing sessions on the GAIA probe, along its Halo L2 orbit. Observations have been carried out with the Cassini 1.52m telescope of the Loiano Observatory (Italy), in a six-months interval along the night of Oct 17-18, 2014 and on March 26-27, 2015. The telescope was equipped with the BFOSC camera, carrying a EEV 1300×1340 px coated and back-illuminated CCD, with a FOV of 12.6×13.0 arcmin, and a pixel scale of 0.58 arcsec px^{-1}.

In addition to a set of eight "white"-light frames (that is by exposing CCD with no photometric filter), the 2014 frames also consisted of six V, R_c, and Gunn z exposures. Overall, the spacecraft was tracked along five hours. The 2015 night was just devoted to a one-shot check of GAIA's position and apparent luminosity in the R_c and V bands. Both nights had photometric conditions along the observation windows, with an R-band FWHM seeing figure about 1.5″-1.7″. The relevant data of our observations are summarized in Table 1. All frames were taken in "on-target" tracking mode, with the only exception of one image (as marked in the table), tracked in sideral mode for the illustrative purpose of Fig. 4.

Table 1: The Oct 17-18, 2014 and March 26-27, 2015 Gaia observations

UTC[a] hh:mm:ss.s	RA[b,c] (J2000) hh:mm:ss.sss	Dec[b,c] dd:mm:ss.ss	Mag[c,d]	Exp.[e] sec
Oct 17-18, 2014 observing session				
20:08:55.5	$01{:}49{:}13.459_{\pm009}$	$+15{:}30{:}11.54_{\pm43}$	$20.6_{\pm3}$ w_R	120 d
20:15:45.6	$01{:}49{:}14.134_{\pm049}$	$+15{:}30{:}20.50_{\pm62}$	$20.7_{\pm3}$ w_R	300 d
20:23:56.1	$01{:}49{:}14.951_{\pm015}$	$+15{:}30{:}31.71_{\pm21}$	$21.1_{\pm3}$ w_R	300 d
20:28:55.5	$01{:}49{:}15.434_{\pm028}$	$+15{:}30{:}38.12_{\pm29}$	$20.9_{\pm3}$ w_R	300 d
20:34:08.3	$01{:}49{:}15.907_{\pm016}$	$+15{:}30{:}45.32_{\pm21}$	$20.6_{\pm3}$ w_R	300 d
20:44:07.5	$01{:}49{:}16.758_{\pm014}$	$+15{:}30{:}57.88_{\pm13}$	$20.9_{\pm3}$ w_R	300 d
20:55:32.7	$01{:}49{:}17.695_{\pm015}$	$+15{:}31{:}11.71_{\pm14}$	$20.5_{\pm3}$ w_R	300 s
21:13:16.1	$01{:}49{:}18.975_{\pm017}$	$+15{:}31{:}34.35_{\pm21}$	$21.0_{\pm2}$ R_c	300 d
21:29:09.9	$01{:}49{:}20.007_{\pm016}$	$+15{:}31{:}52.66_{\pm16}$	$22.2_{\pm2}$ V	420 d
21:35:46.8	$01{:}49{:}20.363_{\pm016}$	$+15{:}32{:}00.45_{\pm54}$	$20.6_{\pm4}$ z_R	300 d
21:44:25.3	$01{:}49{:}20.896_{\pm015}$	$+15{:}32{:}09.63_{\pm09}$	$20.7_{\pm2}$ R_c	300 d
00:50:46.7	$01{:}49{:}29.027_{\pm005}$	$+15{:}34{:}37.50_{\pm34}$	$21.0_{\pm2}$ R_c	300 d
00:58:26.2	$01{:}49{:}29.475_{\pm011}$	$+15{:}34{:}40.94_{\pm25}$	$20.8_{\pm3}$ w_R	300 d
01:10:54.5	$01{:}49{:}30.163_{\pm008}$	$+15{:}34{:}45.55_{\pm27}$	$21.9_{\pm2}$ V	600 d
March 26-27, 2015 observing session				
00:00:14.5	$12{:}28{:}27.063_{\pm013}$	$+04{:}09{:}23.99_{\pm20}$	$20.7_{\pm3}$ R_c	480 d
00:13:46.8	$12{:}28{:}27.499_{\pm013}$	$+04{:}09{:}02.05_{\pm20}$	$21.7_{\pm3}$ V	900 d

[a] Luminosity-weighted time barycenter, according to eq. (9)
[b] Assumed topocentric coordinates of the telescope: $(\lambda, \phi, h) = (11^o20^m02.7^s\ E,\ 44^o15'33.2''\ N, 745.3$ m a.s.l.)
[c] Error figures apply to the last digits of each entry
[d] Photometric bands: Johnson-Cousins bands (V,R_c), R-converted white light (w_R), and Gunn z band (z_R)
[e] Tracking mode: d = differential ("on-target"), s = sideral

In the figure we actually report two consecutive 300 sec exposures of the same field, along the Oct 2014 night, with sideral (left panel) and differential (right panel) telescope tracking on. Just at first glance, it is evident that GAIA can barely be appreciated when trailing across the field, while it clearly stands out when concentrating its light as in the right panel.

3.1. Astrometry

Although limited, our observed database allowed us to benchmark the astrometric and photometric reduction procedure, in order to assess the realistic performance in spatially locating the spacecraft at such large distance from Earth and characterize its apparent photometric properties. A first crucial piece of information deals with astrometry.

For the astrometric solution of the CCD images, after standard reduction procedures with IRAF[2], we relied on the `WCSTools` package[3] to pick up a reference grid of template stars across the field of view and finally set the

[2] See the URLs: *http://iraf.noao.edu.*
[3] See the URLs: *http://tdc-www.harvard.edu/wcstools.*

World Coordinate System (WCS) of the corresponding image. The 50 brightest objects in each field, as detected by the IRAF task `STARFIND`, have been matched by the `WCSTools IMWCS` task with the corresponding HST Guide star Catalogue II (GSC-II) (Russell et al., 1990)[4] available by default to constrain the WCS across the frame. The WCS is the relationship between the pixel coordinates and the celestial coordinate, and it is written in a standard way in the FITS header. The precise astrometric solution is then refined by means of the `WCSTools SCAT` and the `IRAF CCFIND` and `CCMAP` tasks. In particular, `SCAT` retrieves the GSC-II catalogue of the field, while `CCFIND` uses the image WCS to convert the celestial coordinates into image pixel coordinates and refine the latter ones by using a centroid algorithm. The matched coordinates are finally used by `CCMAP` to compute a new plate solution in the RA and DEC domain by a low-order polynomial fit. The astrometric solution is directly inspected by over-plotting the reference catalogue sources on the astrometrically calibrated image.

Overall, our procedure secured an internal astrometric accuracy of $0.38_{\pm 0.18}$ arcsec (rms) in the photometric centroid determination of Gaia's *individual* observations (see Table 1).[5]

Though slightly elongated, the star figures in the telescope images did not prove to severely affect the astrometric solution across the field, provided the trailing intensity of the astrometric calibrators (I) does not vary (or just vary in a predictable way) along the exposure time.[6] This is, actually, a crucial requirement for the photometric barycenter of stellar tracks to consistently tie to the *luminosity-weighted* time barycenter (t_o) of the exposure. By definition, for the latter, we have

$$\frac{t_o}{t_{\rm exp}} = \frac{\int \tau I(\tau) d\tau}{\int I(\tau) d\tau} \frac{1}{\int d\tau} \leq 1. \qquad (9)$$

In case $I(\tau) = \text{const}$, this relationship delivers the obvious solution $t_o = t_{\rm exp}/2$, so that the spacecraft position should be attributed to the mid-exposure time.

Clearly, the attainable astrometric resolution ($\theta_{\rm mas}$) also constrains the required accuracy, $\sigma(t_o)$ in setting t_o, depending on the spacecraft proper motion:

$$\sigma(t_o) \simeq \frac{3.6\,\theta_{\rm mas}}{\zeta} \quad [\text{sec}]. \qquad (10)$$

[4]See the URL: *http://tdc-www.harward.edu/software/catalogues/gsc2.html*.

[5]For the illustrative scope of our analysis, we relied here on the GSC-II catalog, a default reference for `WCSTools` to set the astrometric solution. Other catalogs could, however, be implemented providing to set them in appropriate format. Of these, especially the PPMXL (Roeser, Demleitner, & Schilbach, 2010) and CMC-15 (Niels Bohr Inst. et al., 2014) compilations may prove to be viable alternatives to improve accuracy at least in selected sky regions.

[6]Among others, relevant change along trailing intensity of stars could either be due to any small drift in the sideral and "on-target" telescope tracking, or to any unperceived tiny cloud crossing the field during exposure etc.

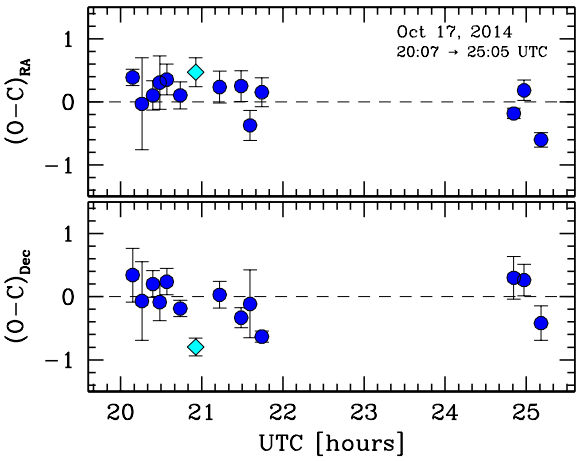

Figure 5: The angular residuals of Gaia's sky path along the night of Oct 17-18, 2014, as seen from the Loiano Observatory (UAI observatory code "598"). The data of Table 1 are compared with the corresponding JPL topocentric ephemeris. Residuals are in arcsec units, both for RA (upper panel) and Dec (lower panel), in the sense "Observed–Computed", (O-C). The only sideral tracking observation in our sample is singled out with a romb marker in both panels.

In the equation, $\theta_{\rm mas}$ is expressed in mas (milliarcsec) unit and ζ in arcsec hr^{-1}, as in Fig. 2. With the Gaia typical figures, t_o has to be known within a few seconds, at most. According to the proper-motion constraints of Fig. 2, this is also the accuracy level for tracking interplanetary spacecraft, while a better tuned clock ($\sigma(t_o) \ll 0.2$ sec) is devised, on the contrary, when observing fast-moving ($\zeta \gg 10^3$) Earth- and Moon-orbiting satellites.

3.1.1. Locating L2 spacecraft

Figure 5 shows that Gaia position consistently compares with its nominal trajectory along the Oct 17, 2014 night, as predicted by the topocentric ephemeris from the JPL Horizons Solar System Dynamics (SSD) Interface.[7] The mean coordinate offsets of our data (in the sense "observed–computed") and their corresponding σ uncertainty amount to (ΔRA, ΔDec) = $(0.10_{\pm 0.08}, -0.09_{\pm 0.10})$ arcsec, which lead to a mean transverse offset $\Delta_{GAIA} = 0.13_{\pm 0.09}$ arcsec. Our observations demonstrate, therefore, that the spacecraft can correctly be located along its expected orbital figure with an angular accuracy θ_{mas} of the order of 90 mas (see Fig. 6).[8] At the reported distance of Gaia along the night (namely $1.39\,10^6$ km, according to the JPL ephemeris), our measures point to a mean orbital offset of $0.9_{\pm 0.6}$ km.

These figures nicely compare also with other almost parallel sets of observations, taken a few nights earlier

[7]See the URL: *http://ssd.jpl.nasa.gov/horizons.cgi*.

[8]Quite consistently, notice that the derived 90 mas rms of the average coordinate residuals of Fig. 6 fully compares with the $(380/\sqrt{N_{\rm obs}}) \sim 100$ mas theoretical figure, as for the independent observations of Table 1.

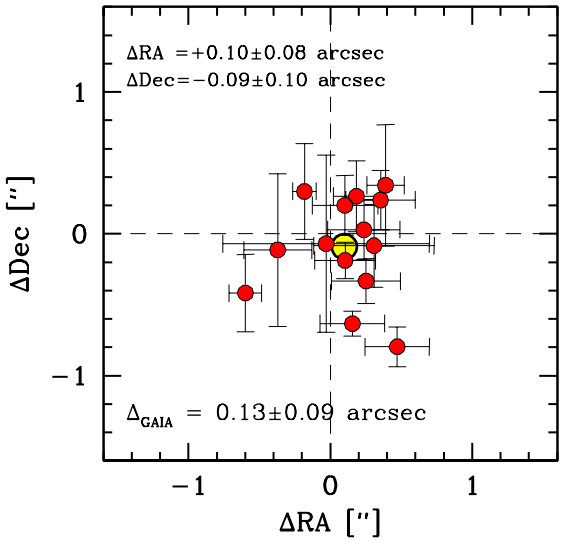

Figure 6: Arcsec coordinate residuals (in the sense "observed–computed") of the Gaia positions along the night of Oct 17, 2014, with respect to the JPL topocentric ephemeris. Mean RA and Dec offsets, together with their 1-σ uncertainty, are reported in the plot. When combined, these lead to a mean path offset with respect to the nominal figure of only $\Delta_{GAIA} = 0.13_{\pm 0.09}$ arcsec (big circle in the plot).

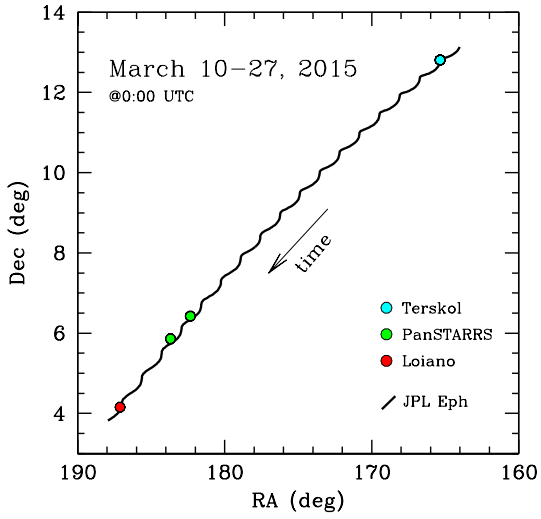

Figure 8: The Gaia sky path along the March 10-26, 2015 period. The Terskol (UAI code "B18") (Velichko et al., 2015, cyan marker), PanSTARRS (UAI code "F51") (Gibson et al., 2015, green dots) and Loiano (red dot) observations are superposed to the JPL topocentric ephemeris (nominally for the B18 location, just as a guideline). Note the daily "ripples" of the Gaia apparent orbit, due to the parallax effect of Earth rotation, that superposes to the overall Lissajous figure on larger scales.

(namely on Oct 14, 2014) by the 1.5m Mt. Lemmon (Kowalski et al., 2014) and the 1.8m LPL Spacewatch II (Tubbiolo, 2014) telescopes. A summary of these data is shown in Fig. 7. After rejecting one clear outlier in the LPL/ Spacewatch II sample, they indicate, overall, a (ΔRA, ΔDec) = $(-0.11_{\pm 0.13}, -0.11_{\pm 0.10})$ arcsec, leading to a mean orbital offset of $\Delta_{GAIA} = 0.16_{\pm 0.11}$ arcsec (or $1.1_{\pm 0.7}$ km) with respect to the corresponding JPL ephemeris.

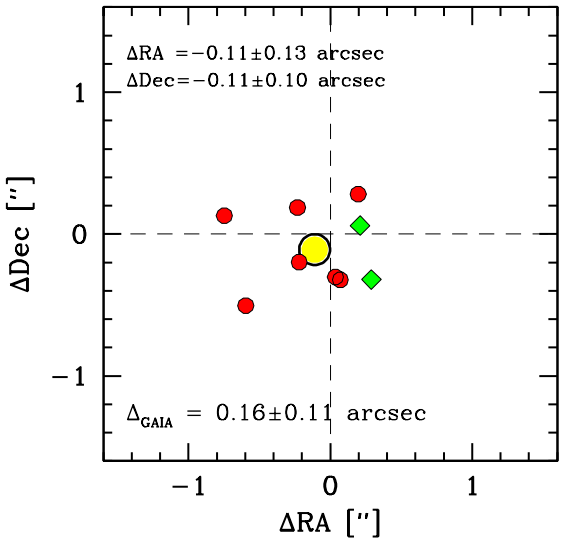

Figure 7: Same as Fig. 6 but for a set of astrometric measurements for the night of Oct 14, 2014, taken with the 1.5m Mt. Lemmon (UAI code "G96") (Kowalski et al., 2014, dots) and the 1.8m LPL/Spacewatch II (UAI code "291") telescopes (Tubbiolo, 2014, rombs). Arcsec coordinate residuals are computed with respect to the correpsonding JPL topocentric ephemeris leading to a mean orbital offset of $\Delta_{GAIA} = 0.16_{\pm 0.11}$ arcsec (big circle in the plot).

Closer to our 2015 observations, a supplementary set of 10 astrometric measurements were provided by Velichko et al. (2015) in the night of March 10, 2015, at the 2m telescope of the Terskol Observatory (Russia), together with six estimates of Gibson et al. (2015) with the 1.8m Pan-STARRS telescope in Haleakala (Hawaii, USA) on the nights of March 23 and 24, 2015 (see Fig. 8).

This coarser set of observations is merged in Fig. 9 with our data and leads, overall, to (ΔRA, ΔDec) = $(0.21_{\pm 0.06}, 0.07_{\pm 0.04})$ arcsec, that is a mean orbital offset of $\Delta_{GAIA} = 0.22_{\pm 0.05}$ arcsec (i.e. $1.6_{\pm 0.4}$ km).

3.1.2. Locating deep-space spacecraft

The brief overview of the Gaia case convincingly supports the preliminary results of the on-going tracking campaign carried on in the framework of the Gaia mission plan (see Altmann et al., 2012, for details), and proves that optical measurements, even carried out with small-class telescopes and under quite standard observing conditions, can easily achieve a superior accuracy when compared to radar tracking, to locate distant spacecraft across the sky. This better score is the obvious consequence of the fact that, for fixed angular resolving power, it must be

$$(\nu\, D)_{\rm radio} \simeq (\nu D)_{\rm opt}\,. \qquad (11)$$

Therefore, if a radar dish is set to operate at some X-band frequency (say 8 GHz, as for the Deep Space Network antennas; Imbriale, 2003), compared to the $\sim 5\,10^{14}$ Hz of a

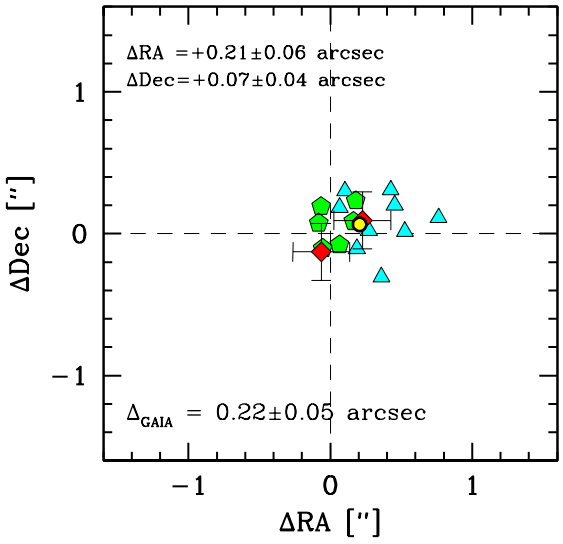

Figure 9: Same as Fig. 6 but for a coarser set of observations taken during March 2015 at the Terskol 2m telescope (triangles), the 1.8m Pan-STARRS telescope (pentagons) and the Loiano 1.52m telescope (rombs, see Table 1). Arcsec coordinate residuals are computed with respect to the appropriate JPL topocentric ephemeris for each observatory. Error bars are only available for our observations, as from Table 1. The merged set of data leads to a mean orbital offset of $\Delta_{GAIA} = 0.22_{\pm 0.05}$ arcsec (yellow circle in the plot) along the spanned period.

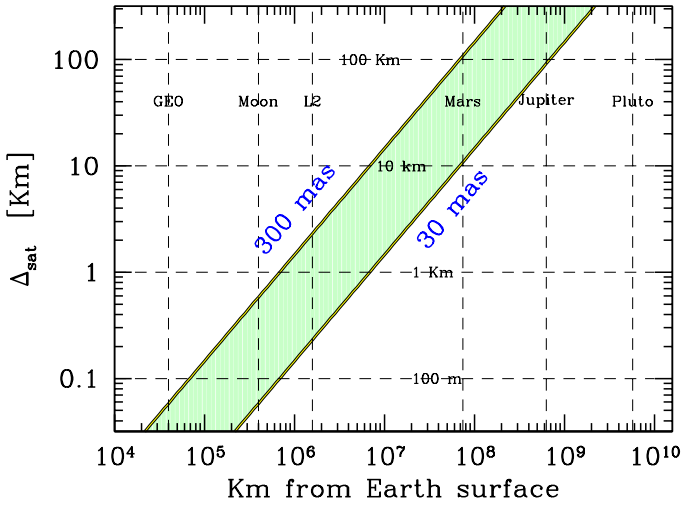

Figure 10: The expected spatial resolution in detecting distant spacecraft within the Solar System. The transverse component, projected on the sky, is assessed in terms of absolute resolution in kilometers at the different distances from Earth. Two representative values for angular resolution of optical tracking are assumed, namely $\theta_{\mu as} = 300$ mas and 30 mas, as labelled on the plot.

telescope observing in the V band, then a factor of $60,000$ larger antenna is required to achieve the same angular performance of the optical instrument. This means that a 60 km-wide(!) antenna (or radio-interferometric baseline) is needed to offset the (diffraction-limited) performance of a 1m telescope.

Clearly, one could argue that any ground-based telescope is eventually seeing (and not diffraction) limited, thus restraining its resolving power to a fraction of arcsec, at best. Another important issue also deals with the inherent astrometric accuracy of reference stars to set the absolute astrometric grid. As for the HST Guide Star Catalog GSC-II used here, currently one of the most populated source of data across the sky for astrometric studies, this limit turns to be about 300 mas (Lasker et al., 2008; Bucciarelli et al., 2008).[9]

On the other hand, multiple measurements are possible of the target differential position with respect to a number of reference (astrometric) stars across the field of view, and this eventually leads to improve target astrometric accuracy by a factor $\sqrt{N_{\rm stars}}$. In addition, further improvements could be envisaged in case a series of independent observations could be collected. Definitely, our Gaia benchmarking showed that an internal accuracy better than 100 mas is a fully attainable goal for standard observations carried out with 2m-class telescopes.

As far as even farther distances from Earth are considered, our arguments lead us to conclude that absolute position of man-made probes could be constrained within a nominal accuracy $\Delta_{\rm sat}$ of the order of

$$\Delta_{\rm sat} = \frac{d_6\,\theta_{\rm mas}}{206} \quad [\rm km], \tag{12}$$

or

$$\Delta_{\rm sat} = 0.72\,u\,\theta_{\rm mas} \quad [\rm km], \tag{13}$$

assuming to express the geocentric distance in million km (d_6) or in AU (u, as in eq. 2), respectively. This relationship is displayed in Fig. 10, for values of $\theta_{\rm mas} = 30$ and 300 mas.

According to the figure, one can hope to optically pinpoint deep-space probes around Mars well within a few tens of km. When complemented with radar information (more effective in ranging measurements and Doppler velocity shift), the optical output could therefore be extremely valuable for an effective 3D location of man-made probes at interplanetary distances.

Quite interestingly, Fig. 10 also suggests that, under appropriate observing conditions (i.e. by masking Moon's overwhelming luminosity), Moon-orbiting spacecraft could be accurately located within a few hundred meters, a precision that could even raise to about 10m in the local framework, for instance when considering station-keeping maneuvering of Earth artificial satellites in geostationary orbit (Montojo, López Moratalla, & Abad, 2011).

[9]The GSC-II provides about 6 reference stars per square arcmin, down to $V \sim 20$, although the reported accuracy refers only to the brightest stars ($V \leq 18.5$) eventually used in our study. This figure is expected to drastically improve (down to $\sim 30\mu$as for $V \sim 15$ stars) in the forthcoming years, just relying on the Gaia star survey (de Bruijne, 2012).

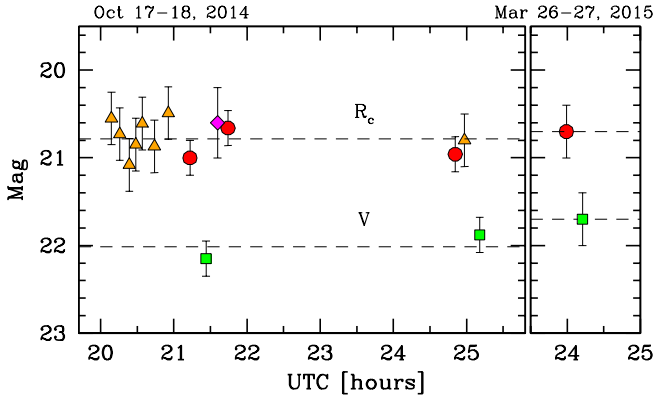

Figure 11: The apparent magnitude of Gaia in different photometric bands along the Oct 2014 and March 2015 observing runs. In addition to R_c (dots) and V (square) Johnson-Cousins bands, "white"-light (triangles) and Gunn z (romb marker) observations have been converted to the R_c magnitude scale as discussed in the text. Dashed lines mark the mean R_c and V magnitude levels.

3.2. Photometry

Both for the 2014 and 2015 observing sessions, photometry in V and R_c bands has been directly calibrated to standard magnitudes by observing two closeby Landolt (1992) fields. Typical rms uncertainty for these observations is 0.2 mag, as summarized in Table 1. Although with a much broader passband, the effective wavelength of the CCD response curve happened to closely match that of the R_c filter ($\lambda_o \simeq 6470$ Å), and this eased a rough but still convenient transformation of the "white" instrumental magnitudes of the Oct 2014 session into pseudo-equivalent R_c figures (called w_R in Table 1). The whole conversion procedure relied on a grid of several field stars in common with the R_c and "white"-light images, and eventually led to a total error of 0.3 mag (rms) for the w_R magnitudes. Just for the sake of comparison, a similar procedure was also applied to the unique Gunn z frame of the 2014 session, leading to a coarser R_c proxy of (i.e. z_R in Table 1), with a 0.4 mag overall error, given a large difference of the z band effective wavelength ($\lambda_o = 9040$ Å).

A plot of all the entries of Table 1 is shown in Fig. 11, versus observing time. Within the photometric accuracy of our observations, along the 2014 session Gaia displayed a constant apparent luminosity with an average magnitude $\langle R_c \rangle = 20.8_{\pm 0.2}$ and $\langle V \rangle = 22.0_{\pm 0.2}$. These results are basically confirmed also by the 2015 observations, taken at the same topocentric distance and phase angle,[10] which indicate $\langle R_c \rangle = 20.7_{\pm 0.2}$ and $\langle V \rangle = 21.7_{\pm 0.2}$. Overall, the observations point to a color of $(V - R_c) = 1.1_{\pm 0.2}$, much redder than the solar value of $(V - R_c)_\odot = 0.4$, as estimated from Pecaut & Mamajek (2013). By itself, this difference suggests that Gaia seems to drastically reprocess the incident solar flux.

Furthermore, our results also point to a much fainter apparent magnitude than originally expected for the spacecraft (namely $R_c \sim$ 17-18, according to Altmann et al., 2011), based on the direct experience on previous L2 missions (especially Wmap and Planck). Yet to a more updated analysis (Altmann et al., 2014), the reason of this discrepancy remains unclear. Evidently, Gaia's faintness and its exceedingly red color have to be related to more inherent reflectance characteristic of the spacecraft structure, especially dealing with the extended Kapton multilayer insulation (MLI) blankets that cover most of the sunshield.

To help better investigate the problem, during the preliminary station-keeping maneuvers of Feb 27 and March 7, 2014, the probe has repeatedly been re-oriented, from its nominal attitude configuration at solar aspect angle[11] $\omega = 45^o$, such as to have its sun-shield directly facing the Sun, that is with $\omega = 0^o$. This greatly brightened Gaia's apparent luminosity up to $R_c^{\rm peak} = 14.5_{\pm 0.2}$ (James, 2014; Jacques et al., 2014; Dupouy & de Vanssay, 2014; Dupouy & Laborde, 2014).

The "face-on" experiment clearly indicated that Gaia's sun-shield reflectance displays an important directional pattern (an effect often referred to as the "opposition surge", e.g. Warell, 2004) with spacecraft luminosity increasing by $\Delta{\rm mag} = 20.8 - 14.5 = 6.3_{\pm 0.3}$ mag when changing ω from 45^o to 0^o. This figure has to be compared with the straight Lambertian prediction, that leads to a much shallower magnitude brightening of

$$\Delta{\rm mag} = -2.5 \log \left(\frac{\cos 45^o}{\cos 0^o} \right) \sim 0.4 \text{ mag}. \qquad (14)$$

3.2.1. Bolometric correction and spacecraft albedo

According to eq. (2), the expected bolometric magnitude of Gaia at the relevant distance of our observations is $Bol = 16.9$ mag.[12] As from eq. (4), this figure can be linked to the apparent R_c magnitude by correcting for the appropriate bolometric correction (BC'_R) and the spacecraft albedo (α). Both these quantities directly relates to the reflectance spectrum of the probe along the entire wavelength range, a feature that can only be poorly known *a priori* and needs to be conveniently assessed "on the fly". For this task, as a part of the characterization checks during the early phases of the Gaia mission (Altmann et al., 2014), narrow-band multicolor photometry was acquired in early 2014 with the Grond imager at the ESO 2.2m telescope in La Silla. This allowed us to reconstruct the spacecraft reflectance spectrum along the 4500-13000 Å wavelength range and therefrom derive the spacecraft colors during the "face-on" experiments and later along the standard operation phase.

[10] The phase angle is the angular distance between Sun (S) and Earth (E), as seen from the probe (P), that is $\phi = \widehat{\rm SPE}$. For our 2014 and 2015 observations $\phi \simeq 7^o$

[11] This is the angle of the incident solar flux with respect to the normal of the satellite planar surface.

[12] We adopt $s = 886$ cm as Gaia's relevant size to be adopted in eq. (2). See: *http://www.esa.int/Our_Activities/Space_Science/Gaia/Gaia_factsheet* for more details.

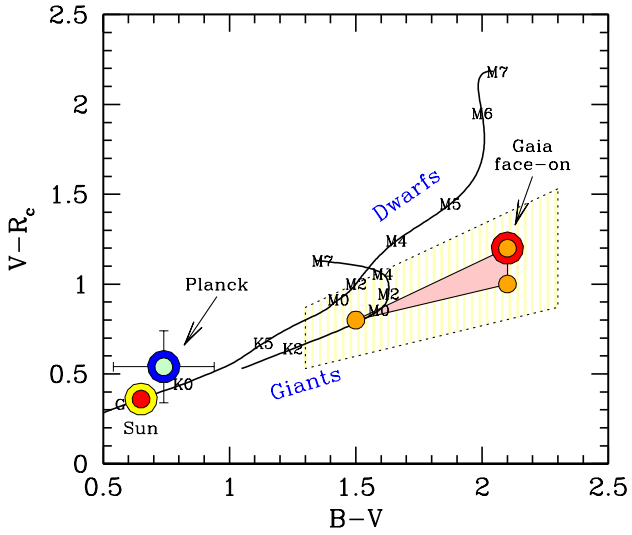

Figure 12: The GAIA color properties, as derived from the GROND reflectance curves of Altmann et al. (2014), are assessed in the $(B-V)$ vs. $(V-R_c)$ plane. The spacecraft location is compared with the stellar locus for dwarf and giant stars of different spectral type (as labelled on the plot), according to Pecaut & Mamajek (2013) and and Houdashelt et al. (2000), respectively. The shaded triangular region on the plot edges the allowed color range of GAIA (including the experimented "face-on" orientation, as discussed in the text), accounting for the reported variability of the spacecraft reflectance. As a reference, the Sun is also marked on the plot, together with the derived colors of the PLANCK probe, according to Altmann et al. (2014).

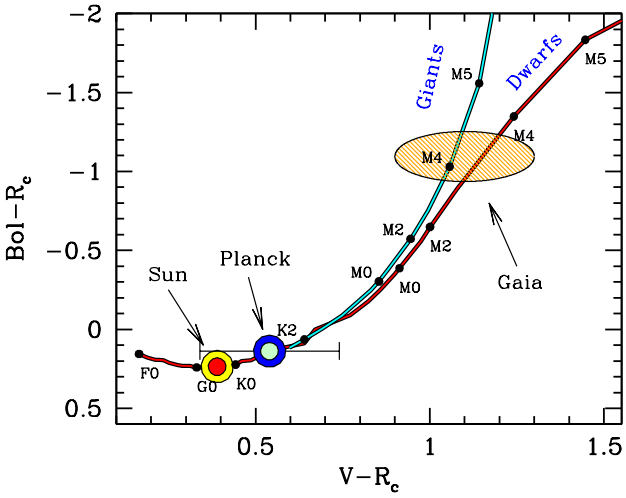

Figure 13: The observed GAIA $(V-R_c)$ color is contrasted in the plot to constrain the spacecraft bolometric correction. As for Fig. 12, the spacecraft location is compared with the stellar locus for dwarf and giant stars of different spectral type (as labelled on the plot), according to Pecaut & Mamajek (2013) and and Houdashelt et al. (2000), respectively, and with the relevant points for the Sun and PLANCK probe.

As far as the $(B-V)$ and the $(V-R_c)$ colors are concerned, the spacecraft location is compared in Fig. 12 with the Sun and the locus for dwarf and giant stars of different spectral type. The empirical compilation of Pecaut & Mamajek (2013) for MK-class V stars is adopted, for this comparison, together with the theoretical models of giant stars from Houdashelt et al. (2000). As a further interesting match, in the figure we also added the colors of PLANCK, as derived from the original reflectance spectrum of Altmann et al. (2014). Contrary to PLANCK, which resulted to be a quite effective proxy of the Sun, GAIA roughly behaves like a red dwarf of very late M spectral type, with an even more depleted B luminosity (i.e. "redder" $B-V$ color). In addition, one has to report from the GROND data, an important (and yet partly unexplained) spectral variability of the probe, with its optical colors actually cornered within the wide region marked in Fig. 12.

On the basis of the reference $(V-R_c)$ color, in Fig. 13 we try to envisage a suitable bolometric correction by comparing, again, with the Pecaut & Mamajek (2013) and Houdashelt et al. (2000) stellar calibrations. Differently from PLANCK, GAIA's color properties point to a much larger correction, that we can tentatively place around a value of $BC'_R \simeq -1.1 \pm 0.2$ mag, although with a large uncertainty, further magnified by the spacecraft spectral variability.

With the relevant figures, under Lambertian assumptions, eq. (4) takes the final form as

$$20.8_{\pm 0.2} - 0.4_{\pm 0.3} = 16.9 + 1.1_{\pm 0.2} - 2.5 \log \alpha, \quad (15)$$

where the apparent R_c magnitude in the l.h. term of the equation has been corrected[13] to $\omega = 0^o$, according to eq. (14). This relationship eventually leads to a nominal value of the GAIA albedo $\alpha = 0.11_{\pm 0.05}$.

Strictly speaking, however, this estimate is most likely to be taken as a *lower limit* for the true Bond albedo, due to sun-shield reflectance anisotropy, as we were discussing before. In fact, by applying our arguments to the real "face-on" spacecraft configuration, one is led to conclude that GAIA *could not be brighter* than $R_c^{\rm peak} \geq 16.9_{\pm 0.3} + 1.1_{\pm 0.2} = 18_{\pm 0.4}$, as originally estimated by Altmann et al. (2011), but evidently at odds with the observed evidence.

4. Probing interplanetary distances

When coupled with previous theoretical arguments, the GAIA observations provide us with a useful tool to consistently size up the required telescope performance in order to detect deep-space probes at even larger distances from Earth, for instance when heading toward other planets of the solar system. If we set a minimum (S/N) threshold for target detection, then eq. (6) (with "on-target" telescope tracking, that is for $\Delta\mu_{\rm sat} = 0$) can be solved to obtain the faintest possible magnitude we could reach and, by means

[13] The error bar on the eq. (14) magnitude correction accounts for the $\pm 15^o$ maximum phase angle excursion of the spacecraft along its libration orbit around L2, as seen from Earth.

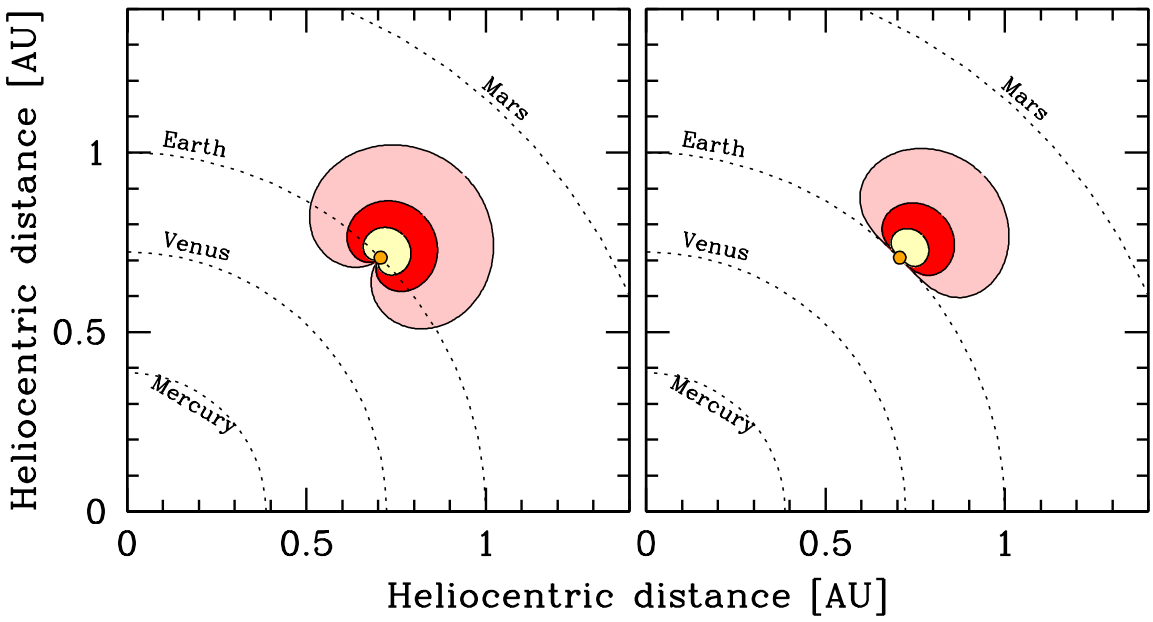

Figure 14: Visibility maps of deep-space probes, as optically tracked from Earth with 1hr CCD exposure by different telescopes. Sky conditions assume a seeing FWHM = 1 arcsec and $\mu^R_{\rm sky} = 20.5$ mag arcsec^{-2}. The GAIA effective area $\mathcal{A} = 10^5$ cm^2 (that is by assuming $\alpha = 0.11$ as a conservative estimate of the true Bond albedo) has been taken as a reference. The marked "horizons" in all panels assume to observe with a 2m (yellow region), 8m (red), and 40m (pink) telescopes, at $(S/N) > 5$ detection threshold. The small orange dot marks Earth's influence sphere (edging the Lagrangian L1 and L2 points), throughout. Left panel refers to the case of a spherical spacecraft, while right panel assumes a prevailing planar structure of the target. Mercury, Venus, Earth, and Mars orbits are sketched, as a guideline.

of eq. (4) and (2), its corresponding maximum geocentric distance.

As probe needs to be under Sun's illumination to be detected from Earth, this also sets a constraint to the allowed range of the phase angle, depending on spacecraft (geocentric) distance and physical structure. If planar components (i.e. large solar panels etc., either facing Earth or Sun) are the prevailing features of the probe, then the simple geometrical arguments outlined in Sec. 3.2 for the case of GAIA indicate that its apparent luminosity under different view angles scales as $\cos(\phi)$. This evidently implies that $|\phi| \leq 90^o$ for the probe to be visible. Much larger values of ϕ may, however, be allowed to roughly spherical shapes, as a cardioid-shaped luminosity law, as $[1 + cos(\phi)]/2$, (e.g. Meeus, 1998) holds in this case.

The visibility map for the illustrative case of either a spheric or straight a planar satellite geometry is sketched in the two panels of Fig. 14, respectively. Calculations have been carried out for the GAIA's effective area $\mathcal{A} = \alpha s^2 \simeq 10^5$ cm^2 (which assumes a conservative albedo value $\alpha = 0.11$) supposing to detect the spacecraft at a (S/N) ratio better than 5. With the 8m-class (or bigger) telescopes currently in use, one sees that an important region can be explored, well beyond the Earth's influence sphere (that embodies the Lagrangian L1 and L2 points) reaching, for instance, distant spacecraft along their initial Hohmann transfer to Mars, up to geocentric distances of some 30 million km (roughly 0.2 AU).

Even 2m-class telescopes could however usefully track deep-space probes, for instance during their flyby approach to Earth for gravity sling toward external planets. Successful observations of the Rosetta spacecraft (Glassmeier et al., 2007), along its 2005 and 2007 gravity-assist maneuvers (e.g. Bedient & Hutsebaut, 2005; Dillon, 2005; Hill et al., 2005; James, 2005; Juels & Holvorcem, 2005; Kusnirak, 2005a,b; Manca & Cavagna, 2005; Stevens, 2005; Ticha & Tichy, 2005; Birtwhistle, 2007a,b,c; Bittesini et al., 2007a,b,c; Donato et al., 2007; Hill et al., 2007a,b; Kowalski et al., 2007)[14] are a relevant example of such a kind of applications. The current Hayabusa 2 mission (Kuninaka et al., 2013) could soon provide another intersting case to benchmark the method.

According to Fig. 14, optical tracking is of lesser point for any space mission toward inner planets (i.e. Venus and Mercury). This is because the orbit geometry leads probes usually to appear from Earth at large phase angles, thus poorly reflecting Sun's light in our direction. An enhanced spacecraft effective area– either in terms of better reflectance to improve the albedo or directly by increasing the physical size of the target, as likely the case of the forthcoming (manned) missions to Mars– could be the obvious issue in this case, as we show in the illustrative case of Fig. 15. By the way, a closer look to Fig. 14 also shows

[14] DASO Circulars are made available in electronic form at the URL: *http://www.minorplanetcenter.net/iau/DASO/DASO.html*.

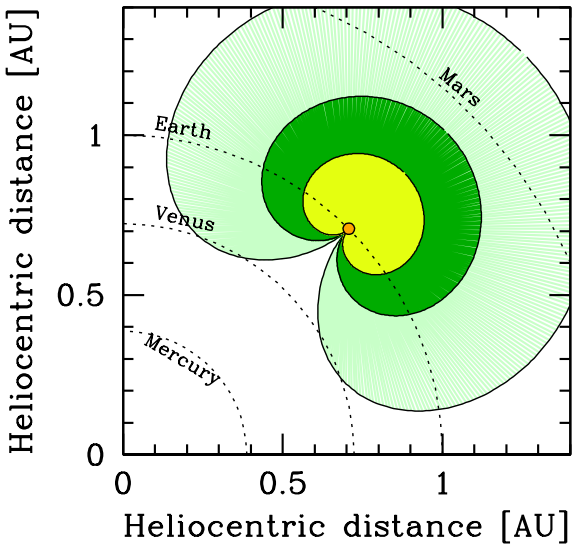

Figure 15: Same as Fig. 14 but for 2m (green), 8m (dark green) and 40m (pale green) telescopes looking (at a $S/N \sim 5$ or better threshold) at a deep-space spherical probe of Gaia's 10× enhanced effective area (namely $\mathcal{A} = 10^6$ cm^2). Under these more favourable circumstances, note that a VLT-class telescope could yet confidently track a spacecraft along most of its Hohmann trajectory to Mars and Venus, while a 2m telescope could, in general, effectively probe distant spacecraft some 40 million km away from Earth.

that spherical spacecraft would better perform than other probes with more planar surfaces.

5. Summary & Conclusions

We assessed in some detail the observing performance of optical telescope-tracking techniques, for accurate characterization of deep-space probes around the Earth-Sun libration point L2 and beyond, toward interplanetary travels. We provided a general estimate of the expected S/N ratio, quantifying the superior improvement of on-target tracking, a mandatory requirement, especially when observing with small-class telescopes.

The current Gaia mission has been taken as a pilot case for our discussion. In this regard, we reported on fresh optical photometry and astrometric results, that led to angularly locate the spacecraft across the sky within $0.13_{\pm 0.09}$ arcsec, or $0.9_{\pm 0.6}$ km. Photometric results also indicate for Gaia a quite red color, with $(V-R_c) = 1.1_{\pm 0.2}$ and an apparent magnitude $R_c = 20.8_{\pm 0.2}$, much fainter than expected and dimmed by a large bolometric correction $(Bol - R_c) = -1.1_{\pm 0.2}$. These features lead to a lower limit for the Bond albedo $\alpha = 0.11_{\pm 0.05}$ and confirm that the unabsorbed fraction of the incident Sun light is strongly reddened by the MLI blankets, that cover the spacecraft sun-shield.

These observations provided us with the reference figures to consistently assess the detection threshold for any deep-space probe toward inner and outer planets of the Solar System. Waiting for next-generation (E-ELT) telescopes, yet VLT-class instruments could be able to track distant spacecraft, like Gaia, along their initial Hohmann transfer to Mars, some 30 million km away. As successfully done with the Rosetta spacecraft, we confirm that even 2m-class telescopes could usefully help track deep-space probes, along their Earth's gravity-assist maneuvers heading interplanetary targets.

We finally demonstrated that optical tracking from 8m ground telescopes could fully flank the standard radar-ranging techniques to probe distant spacecraft along the forthcoming missions to Venus and Mars, providing to deal with (round-shaped) space vehicles of minimum effective area $\mathcal{A} = \alpha s^2 \geq 10^6$ cm^2.

6. Acknowledgements

We would like to acknowledge the timely and very competent review of the two anonymous referees, that greatly helped refine the original version of our study.

This work made extensive use of the IRAF package, written and supported by the National Optical Astronomy Observatories (NOAO) in Tucson, Arizona. NOAO is operated by the Association of Universities for Research in Astronomy (AURA), Inc. under cooperative agreement with the National Science Foundation.

Our astrometric procedure made reference to the GSC-II Catalog, a joint project of the Space Telescope Science Institute (STScI) and the Osservatorio Astronomico di Torino (OATo), Italy. The STScI is operated by AURA under NASA contract NAS5-26555. The participation of OATo is supported by the Italian Council for Research in Astronomy. Additional support is provided by ESO and the Space Telescope European Coordinating Facility, the International GEMINI project and the European Space Agency (ESA).

Part of the data retrieval has been eased by the DEXTER graphic interface, hosted at the German Astrophysical Virtual Observatory (GAVO) in Heidelberg.

We thank Roberto Gualandi and Italo Foppiani at OABo, Italy, for invaluable help along the telescope observations, and Jessica Mink at the Harvard-Smithsonian Center for Astrophysics of Cambridge MA, USA for her kind help to introduce us to the `WCSTools` package.

References

Altmann M., et al., 2011, Proc. of the Workshop Gaia Fun-SSO, in electronic form at *http://www.imcce.fr/langues/en/-publications/colloques/gaiafun/*

Altmann M., et al., 2012, Proc. of the Workshop Gaia Fun-SSO, in electronic form at *http://www.imcce.fr/hosted_sites/-gaiafun2012/*

Altmann M., et al., 2014, SPIE, 9149, 91490P

Barret, D., Nandra, K., Barcons, X., et al. 2013, SF2A-2013: Proc. of the Annual meeting of the French Society of Astronomy and Astrophysics, 447

Bedient J. & Hutsebaut R. 2005, DASO Circ. No. 22, IAU Minor Planet Center, ed. G. V. Williams

Bessell, M. S. 1979, PASP, 91, 589
Birtwhistle P. 2007a, DASO Circ. No. 123, IAU Minor Planet Center, ed. G. V. Williams
Birtwhistle P. 2007b, DASO Circ. No. 124, IAU Minor Planet Center, ed. G. V. Williams
Birtwhistle P. 2007c, DASO Circ. No. 127, IAU Minor Planet Center, ed. G. V. Williams
Bittesini L., et al. 2007a, DASO Circ. No. 125, IAU Minor Planet Center, ed. G. V. Williams
Bittesini L., et al. 2007b, DASO Circ. No. 126, IAU Minor Planet Center, ed. G. V. Williams
Bittesini L., et al. 2007c, DASO Circ. No. 128, IAU Minor Planet Center, ed. G. V. Williams
Bray T. A., Gouclas C. L., 1967, AJ, 72, 202
Bucciarelli B., et al., 2008, IAUS, 248, 316
Buzzoni, A. 2005, MNRAS, 361, 725
Buzzoni, A., Patelli, L., Bellazzini, M., Pecci, F. F., & Oliva, E. 2010, MNRAS, 403, 1592
Cacciari C., 2015, ASSP, 39, 155
de Bruijne, J. H. J. 2012, Ap&SS, 341, 31
Dillon W. G. 2005, DASO Circ. No. 21, IAU Minor Planet Center, ed. G. V. Williams
Donato L., Gonano V., Guido E. & Sostero G. 2007, DASO Circ. No. 129, IAU Minor Planet Center, ed. G. V. Williams
Dupouy, P. & de Vanssay, J. B. 2014, DASO Circ. No. 505, IAU Minor Planet Center, ed. G. V. Williams
Dupouy, P. & Laborde, J. 2014, DASO Circ. No. 507, IAU Minor Planet Center, ed. G. V. Williams
Dutt P., Sharma R. K., 2011, AdSpR, 47, 1894
Farquhar, R. W., & Kamel, A. A. 1973, Celestial Mechanics, 7, 458
Farquhar, R. W., Belbruno, E. A., Dunham, D. W., Guo, Y., & McAdams, J. 2002, IAF abstracts, 34th COSPAR Scientific Assembly, 725
Gardner, J. P., Mather, J. C., Clampin, M., et al. 2006, SSR, 123, 485
Gibson B. et al. 2015, DASO Circ. No. 516, IAU Minor Planet Center, ed. G. V. Williams
Gilmore D. G. 2002, Spacecraft Thermal Control Handbook (Vol. 1), AIAA Series (Reston, USA), ISBN 188498911X
Glassmeier K.-H., Boehnhardt H., Koschny D., Kührt E., Richter I., 2007, SSRv, 128, 1
Hill R. et al. 2005, DASO Circ. No. 22, IAU Minor Planet Center, ed. G. V. Williams
Hill R. E., et al. 2007a, DASO Circ. No. 123, IAU Minor Planet Center, ed. G. V. Williams
Hill R. E., et al. 2007b, DASO Circ. No. 124, IAU Minor Planet Center, ed. G. V. Williams
Houdashelt M. L., Bell R. A., Sweigart A. V., Wing R. F., 2000, AJ, 119, 1424
Imbriale, W. A. 2003, Large Antennas of the Deep Space Network, JPL Deep-Space Comm. and Navigation Ser. (Wiley), ISBN 0471445371
Jacques, C., Pimentel, E. & Barros, J. 2014, DASO Circ. No. 506, IAU Minor Planet Center, ed. G. V. Williams
James N. 2005, DASO Circ. No. 24, IAU Minor Planet Center, ed. G. V. Williams
James, N. 2014, DASO Circ. No. 506, IAU Minor Planet Center, ed. G. V. Williams
Johnson, H. L. 1966, ARA&A, 4, 193
Juels C. W. & Holvorcem P. R. 2005, DASO Circ. No. 24, IAU Minor Planet Center, ed. G. V. Williams
Karttunen, H., Kröger, P., Oja, H., Poutanen, M., Donner, K.J. 1996, Fundamental Astronomy, 3rd ed., Springer-Verlag: Berlin
Kolemen, E., Kasdin, N. J., & Gurfil, P. 2012, Celestial Mechanics and Dynamical Astronomy, 112, 47
Kowalski R. A., et al. 2007, DASO Circ. No. 123, IAU Minor Planet Center, ed. G. V. Williams
Kowalski R. A. et al. 2014, DASO Circ. No. 512, IAU Minor Planet Center, ed. G. V. Williams
Kuninaka H., Hayabusa 2 Project, 2013, LPICo, 1766, 1053
Kusnirak P. 2005a, DASO Circ. No. 20, IAU Minor Planet Center, ed. G. V. Williams
Kusnirak P. 2005b, DASO Circ. No. 23, IAU Minor Planet Center, ed. G. V. Williams
Landolt, A. U. 1992, AJ, 104, 340
Lasker B. M., et al., 2008, AJ, 136, 735
Laureijs, R. J., Duvet, L., Escudero Sanz, I., et al. 2010, Proc. SPIE, 7731, 77311H
Liu, C. B., Hou, X. Y., & Liu, L. 2007, Advances in Space Research, 40, 76
Manca F. & Cavagna M. 2005, DASO Circ. No. 23, IAU Minor Planet Center, ed. G. V. Williams
Meeus J. 1998, Astronomical Algorithms, Richmond: Willmann-Bell, ISBN 0-943396-63-8.
Montojo F. J., López Moratalla T., Abad C., 2011, AdSpR, 47, 1043
Mooney, J. T., Reardon, P. J., Gregory, D., et al. 2006, Proc. SPIE, 6265, 62652W
Nariai K., 1975, A&A, 43, 309
Niels Bohr Institute U. o. C., Inst. of Astronomy C., UK, Real Inst. y Obs. de La Armada en San Fernando, 2014, Carlsberg Meridian Catalog Number 15
Patat, F. 2003, A&Ap, 400, 1183
Pecaut M. J., Mamajek E. E., 2013, ApJS, 208, 9
Qiao, D., Cui, P., Wang, Y., et al. 2014, Advances in Space Research, 54, 2087
Rawal J. J., 1991, EM&P, 54, 283
Roeser S., Demleitner M., Schilbach E., 2010, AJ, 139, 2440
Ruprecht, J. D., Stuart, J. S., Woods, D. F., & Shah, R. Y. 2014, Icarus, 239, 253
Russell, J. L., Lasker, B. M., McLean, B. J., Sturch, C. R., & Jenkner, H. 1990, AJ, 99, 2059
Stevens B. L. 2005, DASO Circ. No. 23, IAU Minor Planet Center, ed. G. V. Williams
Ticha J. & Tichy M. 2005, DASO Circ. No. 25, IAU Minor Planet Center, ed. G. V. Williams
Tubbiolo, A. F. 2014, DASO Circ. No. 512, IAU Minor Planet Center, ed. G. V. Williams
Veis, G. 1963, SSR, 2, 250
Velichko S., Andreev M., Godunova V. 2015, DASO Circ. No. 516, IAU Minor Planet Center, ed. G. V. Williams
Warell J., 2004, Icar, 167, 271
Woods, D. F., Lambour, R. L., Faccenda, W. J., et al. 2014, Proc. SPIE, 9149, 91490S
Zagouras C., Markellos V. V., 1985, CeMec, 35, 257